Materials & Design 185 (2020) 108233

Contents lists available at ScienceDirect

Materials & Design

journal homepage: www.elsevier.com/locate/matdes

Experimental assessment of the microstructure evolution and liquidus projection in the Mo-rich Mo–Si–B system

G. Hasemann [a, c, *], S. Ida [b], L. Zhu [b], T. Iizawa [b], K. Yoshimi [b], M. Krüger [a, c]

[a] *Forschungszentrum Jülich GmbH, Institute of Energy and Climate Research, Microstructure and Properties of Materials (IEK-2), Leo-Brand-Str. 1, 52425, Jülich, Germany*
[b] *Department of Materials Science, Graduate School of Engineering, Tohoku University, Sendai, Miyagi, 980-8579, Japan*
[c] *Otto-von-Guericke University Magdeburg, Institute of Materials and Joining Technology, Universitätsplatz 2, 39106 Magdeburg, Germany*

HIGHLIGHTS

- The liquidus projection of the Mo-rich portion of the Mo-Si-B system has been critically reinvestigated.
- The Alkemade theorem was used to take a closer look into published liquidus projections and solidification sequences.
- A much larger primary solidification area of the Mo_3Si phase was experimentally determined.
- A revised liquidus projection is presented based on the data experimentally obtained in this study.

GRAPHICAL ABSTRACT

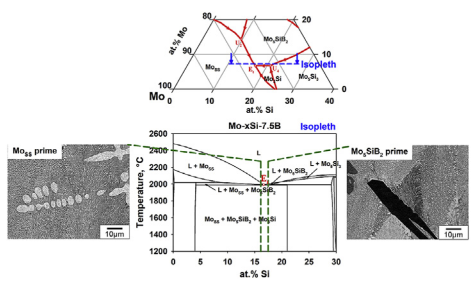

ARTICLE INFO

Article history:
Received 5 August 2019
Received in revised form
20 September 2019
Accepted 24 September 2019
Available online 9 October 2019

Keywords:
Intermetallics
Transition metal alloys and compounds
Microstructure
Scanning electron microscopy
Phase diagrams

ABSTRACT

The present work is focused on a deeper understanding of the microstructure evolution and the solidification reactions of alloys in the Mo-rich portion of the Mo–Si–B system. A number of 59 alloys were selected from the vicinity of the ternary eutectic point to carefully examine the Mo-rich liquidus surface. Therefore, the microstructural evolution of alloy compositions from different primary solidification areas was taken into account. Their solidification path was evaluated by employing the Alkemade theorem. The result is an experimentally based reassessment of the liquidus projection. Special attention had been payed to the Mo_3Si primary solidification area and the Mo_{SS}–Mo_5SiB_2–Mo_3Si ternary eutectic in the Mo-rich portion of the Mo–Si–B system. It could be shown that the primary Mo_3Si phase region is larger as compared to present literature data. The eutectic point could be confirmed to contain 17 ± 1 at.% silicon and 7.5 ± 0.5 at.% boron. As the main outcome from the careful investigation of the solidification paths of numerous alloys a reconstructed liquidus projection is presented.

1. Introduction

Due to the combination of excellent creep behavior and acceptable oxidation resistance at high and ultrahigh temperatures [1–3], molybdenum silicide alloys are seen as very promising candidates for the next generation turbine blade material beyond the capability of state-of-the-art Ni-based superalloys. A US Navy report recently demonstrated capabilities of Mo–Si–B alloys on a hot gas stream static jet engine ring in a fighting plane. According to the report, military aircraft engines realized significant fuel savings of up to 20–40% from jet engine components made of Mo–Si–B

* Corresponding author. Forschungszentrum Jülich GmbH, Institute of Energy and Climate Research, Microstructure and Properties of Materials (IEK-2), Leo-Brand-Str. 1, 52425, Jülich, Germany
E-mail address: georg1.hasemann@ovgu.de (G. Hasemann).

https://doi.org/10.1016/j.matdes.2019.108233

alloys [4]. This shows a future demand of Mo–Si–B engine components not only for military but also for civil aviation. However, scaling up lab production to a higher level of technology readiness is still challenging, i.e. due to the high melting points of various Mo–Si and Mo–B phases which can easily exceed 2000 °C [5]. In terms of relatively low cost casting procedures, binary Mo_{SS}–Mo_5SiB_2 [6–9] and ternary Mo_{SS}–Mo_5SiB_2–Mo_3Si [10–12] eutectic compositions are likely to decrease the melting temperatures of Mo–Si–B alloys and may provide favorable mechanical and oxidative properties due to the unique eutectic microstructure [12].

Beside the isothermal sections of the Mo–Si–B system [13,14], the projection of the liquidus surface provides important information on the solidification reactions and pathways, which can be used to control microstructure evolutions during casting. First investigations on the liquidus projection of the Mo-rich portion of the Mo–Si–B system was presented by Nunes et al. [15]. Based on microstructure observations of arc-melted alloys, they studied the solidification behavior and determined six primary solidification regions in the Mo-rich corner, namely Mo_{SS}, Mo_2B, MoB, Mo_3Si, Mo_5Si_3 and Mo_5SiB_2. Those primary solidification areas are separated by binary eutectic valleys which result in four class II (U-type) and one class I ternary eutectic (referred as E_t) four-phase reactions [15]:

$$L + \beta\text{-MoB} \leftrightarrow Mo_2B + Mo_5SiB_2 \qquad U_1$$

$$L + Mo_2B \leftrightarrow Mo_{SS} + Mo_5SiB_2 \qquad U_2$$

$$L + \beta\text{-MoB} \leftrightarrow Mo_5Si_3 + Mo_5SiB_2 \qquad U_3$$

$$L + Mo_5Si_3 \leftrightarrow Mo_3Si + Mo_5SiB_2 \qquad U_4$$

$$L \leftrightarrow Mo_{SS} + Mo_5SiB_2 + Mo_3Si \qquad E_t$$

However, the chemical composition of their invariant reaction I_1, i.e. the eutectic point, which can be observed in their alloy Mo–13Si–15B had not been further investigated by Nunes et al. [15].

Katrych et al. [16] studied the phase reactions in the Mo–Si–B system at subsolidus temperatures by employing the Pirani-Alterthum melting point method [17] and data obtained by DTA measurements. Compared to Nunes et al. [15], Katrych confirmed the findings to a large extent, except a different solidification sequence, which will be discussed more in detail later on.

Yang and Chang [18,19] redrew the liquidus projection of the Mo-rich corner by using thermodynamic calculations and evaluated earlier literature data by Nunes et al. and Katrych et al. [15,16]. They confirmed the binary eutectic reactions between Mo_{SS} and Mo_5SiB_2 and those between Mo_5Si_3 and Mo_5SiB_2 as well as the ternary eutectic reaction of Mo_{SS}, Mo_3Si and Mo_5SiB_2 which is in agreement with Nunes et al. [15].

Recently, Ha et al. [10] carefully reinvestigated the liquidus surface in Mo-rich Mo–Si–B alloys by employing experimental studies of the binary Mo_{SS}–Mo_5SiB_2 and Mo_3Si–Mo_5SiB_2 eutectics and the ternary eutectic of Mo_{SS}–Mo_5SiB_2–Mo_3Si. They prepared various alloy compositions near the eutectic valleys by arc-melting and their microstructures were investigated carefully and very detailed by using scanning electron microscopy (SEM), electron probe microanalysis (EPMA) and transmission electron microscopy (TEM). Their findings on the eutectic microstructures of Mo_{SS}–Mo_5SiB_2, Mo_{SS}–Mo_3Si–Mo_5SiB_2 and Mo_5SiB_2–Mo_3Si were compared to Yang and Chang's calculated liquidus surface [18,19] and the isothermal section of the phase diagram at 1800 °C [14]. The results obtained by Ha et al. [10] are in very good agreement with Yang and Chang's [18,19] calculations and confirmed their sequence of multiphase reactions during solidification experimentally.

Data on the liquidus projections of this area available from literature are summarized in Fig. 1. In the Mo-rich corner six primary solidification areas are of major interest. The primary solidification areas presented by Yang and Chang [18,19] differ only slightly form that presented by Nunes et al. [15] and Katrych et al. [16] However, the eutectic compositions of Mo_3Si–Mo_5SiB_2 and Mo_{SS}–Mo_5SiB_2–Mo_3Si contain less Si and are enriched in their B concentration as compared to Nunes's and Katrych's approach. Obviously, there are still uncertainties about the size of the primary Mo_3Si solidification area and thus, of the length of the Mo_3Si–Mo_5SiB_2 binary eutectic valley.

In the present work we are focusing on the microstructure formation and chemical composition of the ternary eutectic reaction in the Mo-rich portion of the Mo–Si–B system. The Mo-rich liquidus projection is reinvestigated using experimental data by following and extending Ha et al.'s [10] work. To carry out this work various alloy compositions were chosen to investigate their solidification path and their microstructural evolution. The results will lead to an experimental reassessment of the liquidus projection by paying special attention to the Mo_3Si primary solidification area and the composition of the Mo_{SS}–Mo_5SiB_2–Mo_3Si ternary eutectic in the Mo-rich portion of the Mo–Si–B system.

2. Interpretation of Mo–Si–B liquidus surfaces based on the Alkemade theorem

A short overview of the published liquidus surface projections known for the Mo–Si–B system has been made in the introduction. In the present section, the solidification paths, and thus the sequences of liquid-solid reactions reported in the previous studies [15,16,18,19] are reconsidered and attempted to give universal interpretation on the basis of the Alkemade theorem.

The Alkemade theorem defines the direction of decreasing temperature along a mono-variant reaction line on a liquidus surface [20]. By using Alkemade lines, it is possible to recognize local maxima (more precisely saddle points) along eutectic valleys. Hence, the theorem presents the solidification paths to and from various alloys in one system and is useful to predict possible ternary eutectic reactions. Before applying the Alkemade theorem, it should be noted that the theorem in its original form is specifically defined for line compounds with no (or negligible) solid solubility. On the other hand, many systems show a certain solubility range. Not only binary phases but also the ternary Mo_5SiB_2 phase in the Mo–Si–B system shows an off-stoichiometric compositional range [21,22]. In the present study, it is attempted to apply the Alkemade theorem to the Mo-rich Mo–Si–B system though local maxima may not have been accurately determined in the composition and temperature reported so far. Fig. 2 summarizes the three known liquidus surfaces including the Alkemade line between the stoichiometric Mo_3Si and Mo_5SiB_2 compositions (marked with crosses in Fig. 2) to determine the mono-variant and invariant four-phase equilibria of interest, i.e. Mo_{SS}, Mo_3Si, MoB and Mo_5SiB_2.

At first, a detailed look at Nunes et al.'s [15] and Katrych et al.'s [16] suggested liquidus surfaces will be discussed. Basically, though these two liquidus surface projections fit reasonably well together, it must be emphasized that details of primary phase areas are slightly differing. Katrych et al. postulated the ternary invariant eutectic reaction of L ↔ Mo_3Si + Mo_5Si_3 + Mo_5SiB_2 (donated by their reaction E_1 [16]) was preceded by a mono-variant reaction L + Mo_{SS} ↔ Mo_3Si + Mo_5SiB_2 (denoted by U_5 in their work [16]), while Nunes et al. [15] reported on a mono-variant reaction L + Mo_5Si_3 ↔ Mo_3Si + Mo_5SiB_2 (donated by reaction II_4 in their work [15]) which is followed by the eutectic reaction L ↔ Mo_{SS} + Mo_3Si + Mo_5SiB_2 (donated as reaction I_1 by Nunes et al. [15]

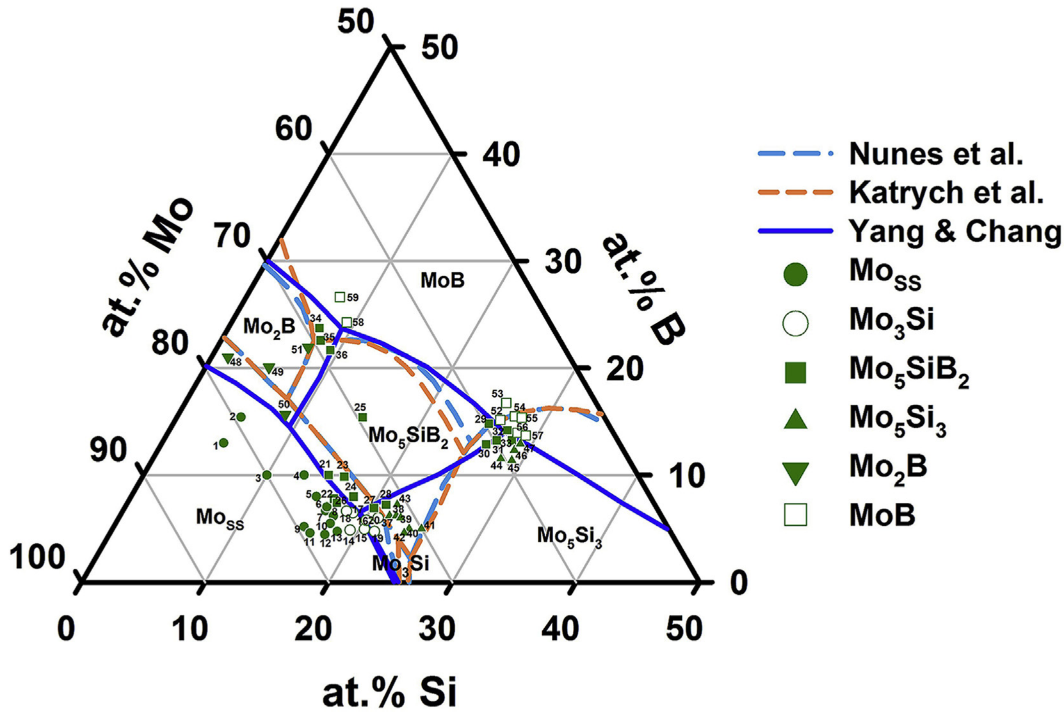

Fig. 1. Alloys investigated in the present work divided into their specific primary solidification phases and compared to the liquidus projections by Nunes et al. [15], Katrych et al. [16] and Yang and Chang [18,19].

and as E_t in the present study). To clarify the difference, the Alkemade line is drawn in Fig. 2 for each individual liquidus surface. According to the theorem, the temperature increases from Mo_3Si (the melting temperature, $T_M^{Mo_3Si}$, is approximately 2025 °C [23]) and from Mo_5SiB_2 ($T_M^{Mo_5SiB_2}$ ~2160–2200 °C [24]) along the Alkemade line, indicating a local maximum (saddle point) on the Mo_3Si–Mo_5SiB_2 binary eutectic valley and that the temperature decreases both to the left and right-hand sides from this saddle point along the mono-variant curve. For the reaction sequences presented by Katrych et al., it is obvious that both the reactions are located on the right hand side of the Alkemade line. Hence, their interpretation of the solidification sequence is in agreement with the theorem, and according to their liquidus projection the ternary eutectic of L ↔ Mo_{SS} + Mo_3Si + Mo_5SiB_2 is impossible. However, this type of reaction was experimentally confirmed by Nunes et al. [15] and further corroborated by Ha et al. [10]. Drawing the same Alkemade line on the liquidus surface projection reported by Nunes et al. [15] shows that the mono-variant reaction of L + Mo_5Si_3 ↔ Mo_3Si + Mo_5SiB_2 is on the right hand side and the invariant reaction of L ↔ Mo_{SS} + Mo_3Si + Mo_5SiB_2 is on the left hand side of the Alkemade line, and that the solidification sequence via these two reactions is indeed possible. Since both the versions differ only slightly and both reactions L + Mo_{SS} ↔ Mo_3Si and L ↔ Mo_3Si + Mo_5Si_3 in the binary Mo–Si system are similar, the crucial point is where either Nunes et al. or Katrych et al. had located their invariant ternary eutectic point. This is aggravated by the fact that the solidification sequence postulated by Katrych et al. is quite doubtful, even if the Alkemade theorem is used correctly. Katrych et al. [16] seem to use the same Si concentration (i.e. the maximum solubility in Mo) for their Mo–Si binary system as compared to Nunes et al. However, in their Fig. 2 the binary eutectic reaction L ↔ Mo_3Si + Mo_5Si_3 has a higher temperature (2030 °C) than the peritectic reaction L + Mo_{SS} ↔ Mo_3Si (2025 °C) [16], which cannot be explained from a thermodynamic point of view. If the peritectic formation of Mo_3Si takes place at 2025 °C, it cannot exist at even higher temperatures - not to mention taking part in a eutectic

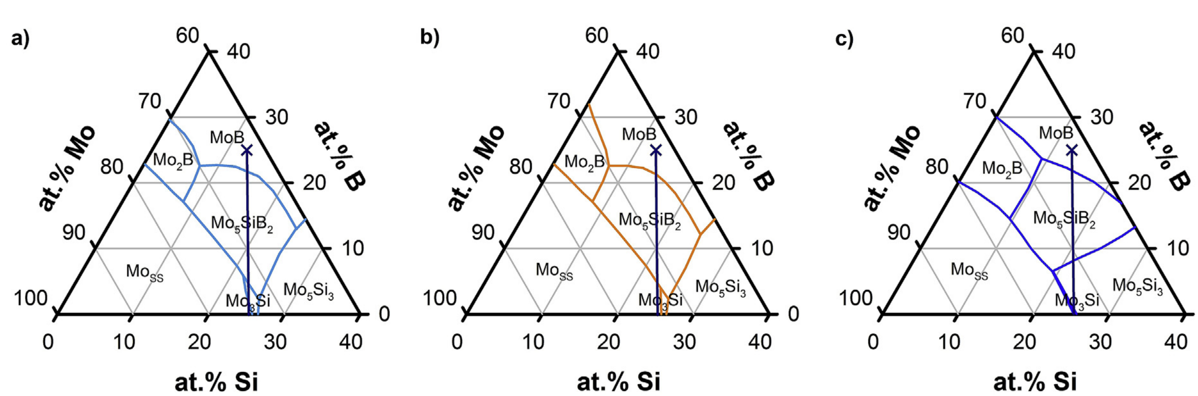

Fig. 2. Alkemade line between the stoichiometric Mo_3Si and Mo_5SiB_2 compositions in the respective liquidus surface projections reported by a) Nunes et al. [15], b) Katrych et al. [16] and c) Yang and Chang [18,19].

reaction at 2030 °C. This would suggest that the peritectic formation would be preferred over the eutectic reaction and arise the question where the liquid phase would come from to form the peritectic in this case. Obviously, there are still uncertainties about the reaction sequence during cooling, if Nunes et al. and Katrych et al. are compared to each other.

However, thermodynamic calculations provided by Yang and Chang [18,19] can shed more light into the situation. The corresponding Alkemade line again connecting the stoichiometric composition of Mo_5SiB_2 (marked with a cross) with Mo_3Si is shown in Fig. 2c). Due to the large primary solidification range of Mo_5SiB_2, the Alkemade line does not intersect with the corresponding Mo_5SiB_2–Mo_3Si eutectic line. Nevertheless, the eutectic line can then be extended until it intersects with the Alkemade line [20,25]. In agreement with the theorem the temperature is decreasing left and right of the Alkemade line. Hence, the solidification sequence can now be interpreted as Nunes et al. [15] suggested and which had been confirmed experimentally by Ha et al. [10]: the ternary eutectic reaction L $\leftrightarrow$ Mo_{SS} + Mo_3Si + Mo_5SiB_2 is preceded by a mono-variant reaction L + Mo_5Si_3 $\leftrightarrow$ Mo_3Si + Mo_5SiB_2, respectively, since both reactions are located clearly on the left hand side of the Alkemade line.

As a conclusion of this paragraph one can state that it might be very difficult to analyze the solidification path of the alloys in the vicinity of the ternary eutectic point. Due to steep slopes of the Mo_{SS} liquidus surface and the shallow characteristic of the Mo_3Si and Mo_5SiB_2 primary solidification surface, undercooling will have an essential influence on the microstructure evolution. Consequently, it seems to be nearly impossible to precisely determine the ternary eutectic Mo_{SS}–Mo_5SiB_2–Mo_3Si composition. This has to be kept in mind when discussing and evaluating the microstructures in their as-cast condition in the following section.

3. Experimental procedure

Near-eutectic Mo–Si–B alloys were produced by conventional arc-melting (AM) of elemental starting materials in an argon atmosphere. To produce buttons of approximately 10–30 g high purity chips or lumps were used. Prior to arc-melting the furnace chamber was evacuated and purged with Ar several times. Prior to melting, a pure titanium target had been used to getter remaining O_2 and N_2 gases in the furnace chamber. To ensure good homogeneity, each button was flipped and remelted more than three times by turning it over before repeated melting. The chemical alloy compositions were verified using inductively coupled plasma optical emission spectroscopy (ICP-OES).

To investigate the microstructures, samples were cut to small pieces via electrical discharge machining (EDM). After subsequently grinding, the specimens were finished by polishing with 3 μm and 1 μm diamond suspension. The microstructural observations were carried out using a scanning electron microscope (SEM) Zeiss Merlin (equipped with an energy-dispersive X-ray spectroscope (EDS) by Oxford Instruments) or a JEOL JSM-7800F. The SEM images were typically obtained in the backscattered electron (BSE) mode. EPMA measurements to determine the chemical composition of each phase and the eutectic structures in the as-cast and annealed state (spot analyses) were carried out using a JEOL JXA-8100. Pure elements of Mo, Si and B were used as standards for the EPMA measurement. The relative error of the resulting compositions is 1%. For phase identification of the as-cast specimens X-ray diffraction (XRD) analysis was carried out using a Bruker D-8 advanced diffractometer and Cu Kα radiation.

4. Results

In the following sections the six primary solidification areas identified by Nunes et al. [15] will be reinvestigated experimentally. To carry out this work, as set of different alloys compositions were chosen in the individual primary phase regions, Fig. 1, and their microstructure evolution will be discussed. Special attention was payed to the Mo_3Si primary solidification area as well as to the four-phase reactions U_3, U_4 and E_t as referred to Nunes et al. [15].

4.1. Alloys with Mo_{SS} primary phase

The Mo_{SS} primary solidification region is adjacent to the binary eutectic reaction of L $\leftrightarrow$ Mo_{SS} + Mo_2B and the peritectic L + Mo_{SS} $\leftrightarrow$ Mo_3Si reaction in the Mo–Si system. Thus, following both mono-variant two-phase lines into the ternary system leads to the four-phase equilibrium points of either the mono-variant U_2 reaction or the invariant ternary eutectic E_t reaction, respectively. Both four-phase reactions are connected via the two-phase Mo_{SS}–Mo_5SiB_2 eutectic valley. The chemical concentrations of the alloys and phases obtained by EPMA and determined by XRD investigated in this primary solidification area are listed in Table 1, respectively.

Exemplarily, Fig. 3 shows the as-cast microstructures of alloys taken from the Mo_{SS} primary solidification region.

Alloy Mo–5.2Si–15.4B (#2) shows relatively large primary Mo_{SS} dendrites, Fig. 3a). The Mo_{SS} phase has a preference to solve Si, which enriches the remaining liquid in its B concentration and shifts the B/Si ratio to higher values. As a result the mono-variant eutectic Mo_{SS}–Mo_2B can be observed. The B/Si ratio in the liquid phases is thus, reduced as the solidification path follows the Mo_{SS}–Mo_5SiB_2 two-phase eutectic valley. This reaction further reduces the B/Si ratio until in a final solidification step the ternary eutectic reaction L $\leftrightarrow$ Mo_{SS} + Mo_5SiB_2 + Mo_3Si is reached. The microstructure observation of alloy Mo–5.2Si–15.4B (#2) are in absolute consistency with investigations by Nunes et al. [15] who were using a similar alloy composition of Mo–5Si–10B (their alloy #39).

After the primary formation of Mo_{SS}, the microstructure evolution of alloy Mo–15Si–8B (#5) continues along the mono-variant binary eutectic valley of Mo_{SS}–Mo_5SiB_2 and the remaining melt solidifies within the invariant ternary eutectic reaction of Mo_{SS}–Mo_5SiB_2–Mo_3Si, according to the microstructure shown in Fig. 3b).

The microstructure of alloys Mo–16.4Si–6.7B (#6) in Fig. 3c) shows only a few primary crystals and a small fraction of two-phase Mo_5SiB_2–Mo_3Si eutectics. Mainly ternary eutectic grains can be observed throughout the entire microstructure, which indicates that alloy Mo–16.4Si–6.7B (#6) can be considered as near-eutectic alloy, respectively.

The microstructure evolution of alloy Mo–18.3Si–4.7B (#13) in Fig. 3d) shows a secondary solidification of Mo_3Si after primary solidification of the Mo_{SS} phase, which is mainly attributed to heavy undercooling effects via arc-melting in a water chilled copper crucible. From this point on the two-phase Mo_5SiB_2–Mo_3Si eutectic is preceding the formation of ternary eutectic Mo_{SS}–Mo_5SiB_2–Mo_3Si grains. Such undercooling effects had been observed and reported before which can lead to the formation of e.g. a two-phase halo surrounding a primary phase indicating non-equilibrium solidification [26,27] or secondary solidification [28]. A similar microstructure had been reported recently [11], which is in agreement of the present results.

4.2. Alloys with Mo_3Si primary phase

The primary field of Mo_3Si seems to be relatively small and is described to not expand deeply into the ternary system [15,16,18,19]. However, the experimental data by Nunes et al. [15] and Katrych et al. [16] suggest a larger expansion of the primary

Table 1
Arc-melted alloys solidifying with the Mo_{SS} primary phase.

Alloy #	at.% Si	at.% B	Primary Mo_{SS} + further solidifying phases	Phases by XRD
1	5.0	13.0	+ Mo_{SS}–Mo_2B + Mo_{SS}–Mo_5SiB_2 + Mo_{SS}–Mo_5SiB_2–Mo_3Si	Mo_{SS} + Mo_3Si + Mo_5SiB_2 + Mo_2B
2	5.2	15.4	+ Mo_{SS}–Mo_2B + Mo_{SS}–Mo_5SiB_2 + Mo_{SS}–Mo_5SiB_2–Mo_3Si	Mo_{SS} + Mo_3Si + Mo_5SiB_2 + Mo_2B
3	10.0	10.0	+ Mo_{SS}–Mo_5SiB_2 + Mo_{SS}–Mo_5SiB_2–Mo_3Si	Mo_{SS} + Mo_3Si + Mo_5SiB_2
4	13.0	10.0	+ Mo_{SS}–Mo_5SiB_2 + Mo_{SS}–Mo_5SiB_2–Mo_3Si	Mo_{SS} + Mo_3Si + Mo_5SiB_2
5	15.0	8.0	+ Mo_{SS}–Mo_5SiB_2 + Mo_{SS}–Mo_5SiB_2–Mo_3Si	Mo_{SS} + Mo_3Si + Mo_5SiB_2
6	16.4	6.7	+ little Mo_3Si–Mo_5SiB_2 + Mo_{SS}–Mo_5SiB_2–Mo_3Si	Mo_{SS} + Mo_3Si + Mo_5SiB_2
7	16.3	7.0	+ little Mo_3Si–Mo_5SiB_2 + Mo_{SS}–Mo_5SiB_2–Mo_3Si	Mo_{SS} + Mo_3Si + Mo_5SiB_2
8	17.3	6.2	+ Mo_3Si–Mo_5SiB_2 + Mo_{SS}–Mo_5SiB_2–Mo_3Si	Mo_{SS} + Mo_3Si + Mo_5SiB_2
9	15.4	5.2	+ Mo_3Si–Mo_5SiB_2 + little Mo_{SS}–Mo_5SiB_2–Mo_3Si	Mo_{SS} + Mo_3Si + Mo_5SiB_2
10	17.4	5.5	+ Mo_3Si + Mo_3Si– Mo_5SiB_2 + little Mo_{SS}–Mo_5SiB_2–Mo_3Si	Mo_{SS} + Mo_3Si + Mo_5SiB_2
11	16.2	4.6	+ Mo_3Si + Mo_3Si–Mo_5SiB_2 + little Mo_{SS}–Mo_5SiB_2–Mo_3Si	Mo_{SS} + Mo_3Si + Mo_5SiB_2
12	17.5	4.4	+ Mo_3Si + little Mo_3Si–Mo_5SiB_2 + Mo_{SS}–Mo_5SiB_2–Mo_3Si	Mo_{SS} + Mo_3Si + Mo_5SiB_2
13	18.3	4.7	+ Mo_3Si + little Mo_3Si–Mo_5SiB_2 + Mo_{SS}–Mo_5SiB_2–Mo_3Si	Mo_{SS} + Mo_3Si + Mo_5SiB_2

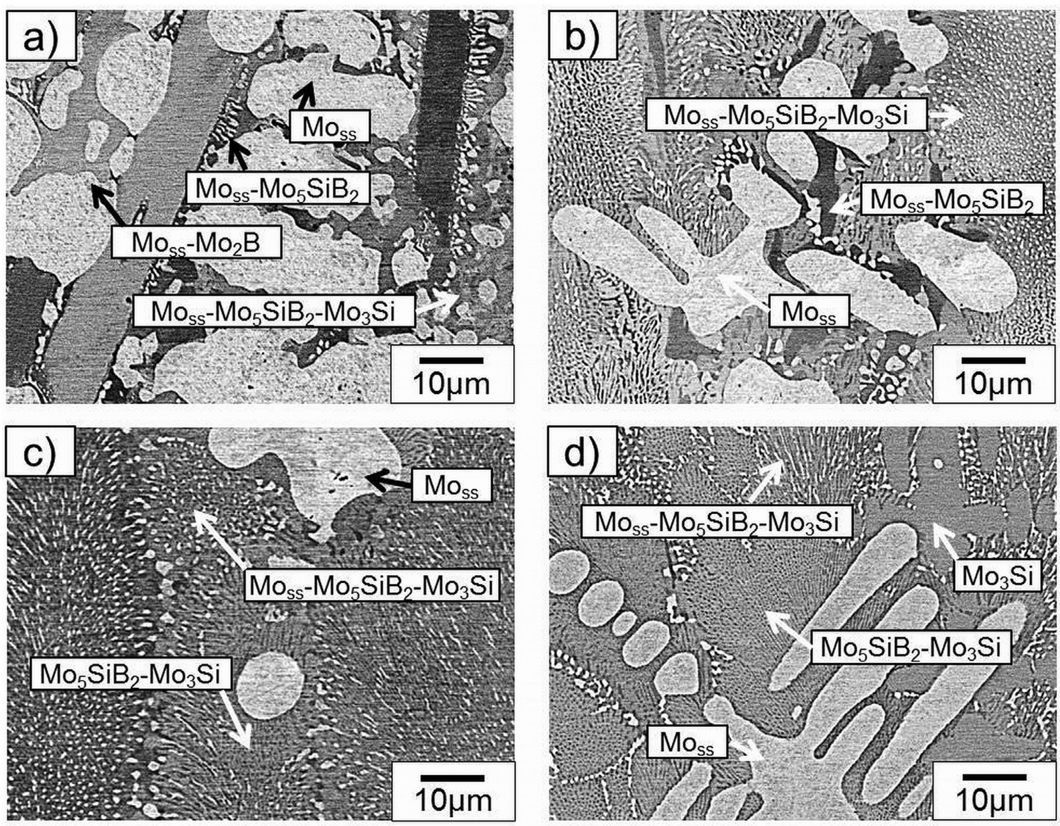

Fig. 3. SEM-BSE images of a) Mo–5.2Si–15.4B (#2), b) Mo–15Si–8B (#5), c) Mo–16.4Si–6.7B (#6) and d) Mo–18.3Si–4.7B (#13).

field along the Si axis (reaching a maximum following the Mo_5SiB_2–Mo_3Si mono-variant line), while the thermodynamic calculations by Yang and Chang [18,19] would imply less Si (about 1 at.%) but reaching deeper into the B-rich direction (≈7 at.%), Fig. 1.

The alloys showing primary solidification in this particular area are summarized in Table 2 and Fig. 4 exemplarily illustrates their respective microstructures after casting.

According to Fig. 4a and b, the microstructure evolution of the alloys Mo–20.4Si–5B (#15) and Mo–18.1Si–6.6B (#18) tend to solidify via identical solidification paths. After the primary Mo_3Si

Table 2
Arc-melted alloys solidifying with the Mo_3Si primary phase.

Alloy #	at.% Si	at.% B	Primary Mo_3Si + further solidifying phases	Phases by XRD
14	19.3	4.9	+ little Mo_5SiB_2–Mo_3Si + Mo_{SS}–Mo_5SiB_2–Mo_3Si	Mo_{SS} + Mo_3Si + Mo_5SiB_2
15	20.4	5.0	+ Mo_5SiB_2–Mo_3Si + Mo_{SS}–Mo_5SiB_2–Mo_3Si	Mo_{SS} + Mo_3Si + Mo_5SiB_2
16	20.2	5.8	+ Mo_5SiB_2–Mo_3Si + little Mo_{SS}–Mo_5SiB_2–Mo_3Si	Mo_{SS} + Mo_3Si + Mo_5SiB_2
17	18.7	6.5	+ Mo_5SiB_2–Mo_3Si + little Mo_{SS}–Mo_5SiB_2–Mo_3Si	Mo_{SS} + Mo_3Si + Mo_5SiB_{22}
18	18.1	6.3	+ little Mo_5SiB_2–Mo_3Si + Mo_{SS}–Mo_5SiB_2–Mo_3Si	Mo_{SS} + Mo_3Si + Mo_5SiB_2
19	21.3	4.7	+ Mo_5SiB_2–Mo_3Si	Mo_3Si + Mo_5SiB_2
20	21.0	6.0	+ Mo_5SiB_2–Mo_3Si	Mo_3Si + Mo_5SiB_2

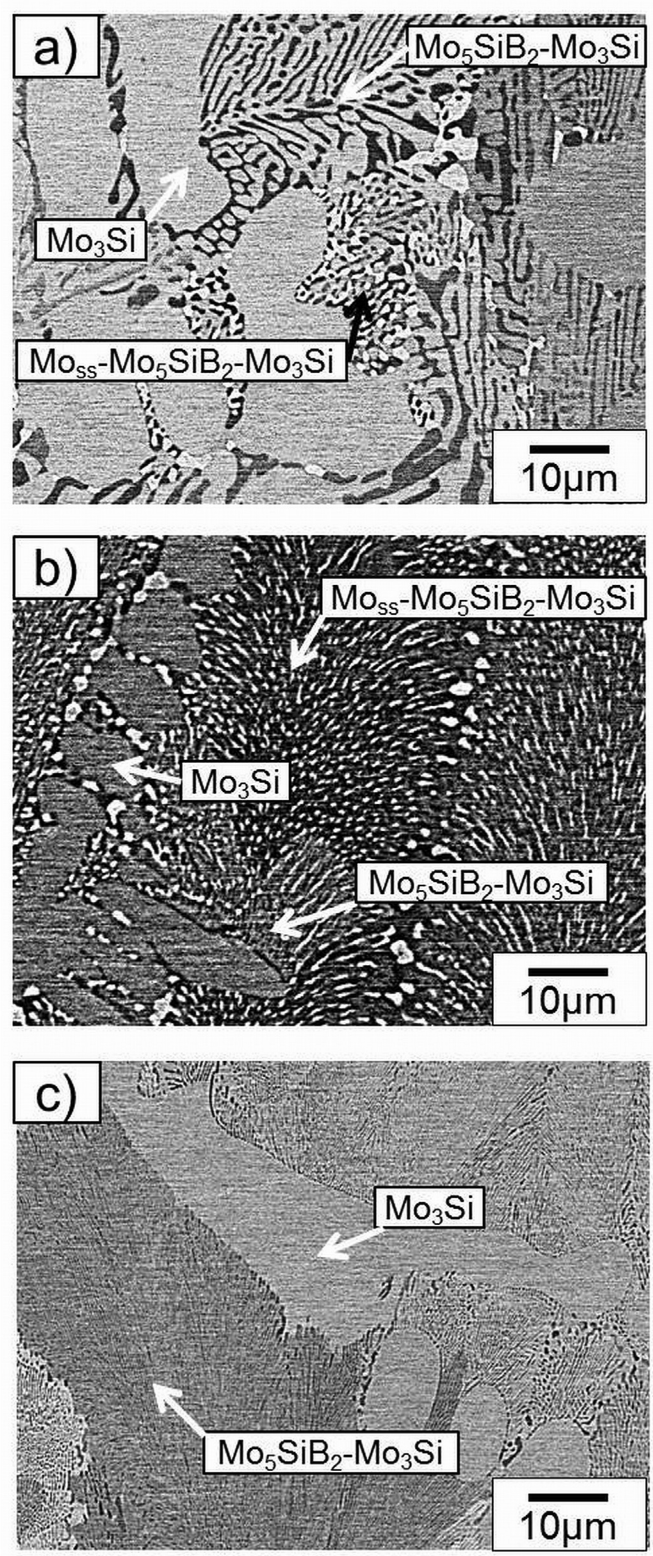

Fig. 4. SEM-BSE images of a) Mo–20.4Si–5B (#15), b) Mo–18.1Si–6.6B (#18) and c) Mo–21Si–6B (#20).

dendrites have formed the solidification proceeds via a two-phase Mo_5SiB_2–Mo_3Si eutectic. The remaining melt undergoes the ternary eutectic reaction E_t, which results in smaller ternary eutectic areas in alloy Mo–20.4Si–5B (#15) relative to alloy Mo–18.1Si–6.6B (#18). Since mostly ternary eutectic areas and only small areas of the two-phase eutectic were observed in alloys Mo–18.1Si–6.6B (#18), this alloy is considered to be very close to the ternary eutectic point within the Mo_3Si primary solidification field. The solidification sequence and microstructure appearance are consistent with recent investigation [11] showing similar microstructures as in the present Fig. 4b.

In opposite, the alloy Mo–21Si–6B (#20), Fig. 4c, should be located clearly within the primary Mo_3Si solidification field since large Mo_3Si dendrites can be observed preceding the Mo_5SiB_2–Mo_3Si reaction. The solidification sequence ends at this two-phase reaction since no Mo_{SS} phases and thus ternary eutectic grains were observed via SEM or XRD.

Based on the present microstructure observations and according to Nunes et al. [15] the lowest point on the Mo_3Si primary surface is the invariant ternary eutectic reaction Mo_{SS}–Mo_5SiB_2–Mo_3Si. Thus, a transformation from the peritectic L + Mo_{SS} ↔ Mo_3Si to a mono-variant eutectic reaction L ↔ Mo_{SS} + Mo_3Si has to occur. However, due to possible undercooling effects and the shallow character of the Mo_3Si liquidus surface it might be possible, that such a mono-variant eutectic reaction may not be observed. Thus, even alloys which are located quite closely to that line, e.g. alloys Mo–19.3Si–4.9B (#14), seem to take cooling paths via the Mo_5SiB_2–Mo_3Si and Mo_{SS}–Mo_5SiB_2–Mo_3Si reactions.

4.3. Alloys with Mo_5SiB_2 primary phase

Alloys which are taken from the Mo_5SiB_2 primary solidification region are listed in Table 3. This region is bound by the two-phase saturation curves U_1–U_2, U_2–E_t, E_t–U_4 and U_4–U_3. The Mo_5SiB_2 stoichiometric composition (Mo–12.5Si–25B) is excluded from its primary solidification field, which has major influence on the synthesis of this phase, especially via melting processes. Technically this means that it is impossible to produce a single phase Mo_5SiB_2 via casting [6]. Furthermore, the pseudo-binary cut along the Mo_{SS}–Mo_5SiB_2 two-phase region reveals that the Mo solubility in Mo_5SiB_2 decreases with decreasing temperature [22] and Mo_{SS} precipitations form during long-term annealing.

Fig. 5a shows the microstructure of alloy Mo–15Si–10B (#21). After the primary Mo_5SiB_2 crystal has formed, the alloy proceeds to solidify via the comparably coarse two-phase mono-variant Mo_{SS}–Mo_5SiB_2 eutectic and a fine ternary eutectic of Mo_{SS}–Mo_5SiB_2–Mo_3Si. The cooling path is in agreement with previous investigations by Ha et al. [10] and corroborates their solidification sequence.

The alloy Mo–16.9Si–7.4B (#26) in Fig. 5b is located close to the ternary eutectic point E_t. The alloy solidifies via the mono-variant Mo_5SiB_2–Mo_3Si two-phase reaction preceding the ternary eutectic reaction between the phases Mo_{SS}, Mo_5SiB_2 and Mo_3Si. In very good agreement with previous work [10,11], the alloy Mo–16.9Si–7.4B (#26) can be treated as near-eutectic alloy.

Alloy Mo–21Si–7.2B (#28) is very close to the class II type reaction U_4. Thus, minor secondary formation of Mo_5Si_3 can be observed in the microstructure in Fig. 5c) but mostly the two-phase Mo_5SiB_2–Mo_3Si eutectic has formed after solidification from the liquid state.

Fig. 5d shows the microstructure of alloys Mo–9.3Si–21.7B (#36). After the primary Mo_5SiB_2 crystal has formed, the alloy proceeds to solidify via the relatively coarse two-phase mono-variant Mo_{SS}–Mo_5SiB_2 eutectic and a fine ternary eutectic of Mo_{SS}–Mo_5SiB_2–Mo_3Si. The shallow Mo_5SiB_2 liquidus surface seems to avoid the class II reaction of L + Mo_2B ↔ Mo_{SS} + Mo_5SiB_2 and thus, the Mo_2B–Mo_5SiB_2 valley.

4.4. Alloys with Mo_5Si_3 primary phase

Alloys which can be attributed to the primary Mo_5Si_3 region are

Table 3
Arc-melted alloys solidifying with the Mo_5SiB_2 primary phase.

Alloy	at.% Si	at.% B	Primary Mo_5SiB_2+ further solidifying phases	Phases by XRD
21	15.0	10.0	+ Mo_{SS}–Mo_5SiB_2 + Mo_{SS}–Mo_5SiB_2–Mo_3Si	Mo_{SS} + Mo_3Si + Mo_5SiB_2
22	16.5	7.8	+ Mo_{SS}–Mo_5SiB_2 + Mo_{SS}–Mo_5SiB_2–Mo_3Si	Mo_{SS} + Mo_3Si + Mo_5SiB_2
23	16.3	9.9	+ Mo_5SiB_2–Mo_3Si + Mo_{SS}–Mo_5SiB_2–Mo_3Si	Mo_{SS} + Mo_3Si + Mo_5SiB_2
24	18.0	8.0	+ Mo_5SiB_2–Mo_3Si + Mo_{SS}–Mo_5SiB_2–Mo_3Si	Mo_{SS} + Mo_3Si + Mo_5SiB_2
25	15.0	15.4	+ little Mo_5SiB_2–Mo_3Si + Mo_{SS}–Mo_5SiB_2–Mo_3Si	Mo_{SS} + Mo_3Si + Mo_5SiB_2
26	16.9	7.4	+ little Mo_5SiB_2–Mo_3Si + Mo_{SS}–Mo_5SiB_2–Mo_3Si	Mo_{SS} + Mo_3Si + Mo_5SiB_2
27	20.2	6.9	+ Mo_5SiB_2–Mo_3Si + little Mo_{SS}–Mo_5SiB_2–Mo_3Si	Mo_3Si + Mo_5Si_3 + Mo_5SiB_2
28	21.0	7.2	+ Mo_5SiB_2–Mo_3Si + little Mo_5Si_3	Mo_5Si_3 + Mo_5SiB_2 + Mo_3Si
29	25.5	14.8	+ Mo_5Si_3–MoB + v-Mo_5SiB_2 + little Mo_5Si_3–MoB–$MoSi_2$	Mo_5Si_3 + Mo_5SiB_2 + MoB + $MoSi_2$
30	26.3	12.9	+ Mo_5Si_3–MoB + Mo_5Si_3–Mo_5SiB_2 + little Mo_5Si_3–MoB–$MoSi_2$	Mo_5Si_3 + Mo_5SiB_2 + MoB + $MoSi_2$
31	26.9	13.3	+ Mo_5Si_3–MoB + Mo_5Si_3–Mo_5SiB_2 + little Mo_5Si_3–MoB–$MoSi_2$	Mo_5Si_3 + Mo_5SiB_2 + MoB + $MoSi_2$
32	27.3	14.2	+ Mo_5Si_3–MoB + Mo_5Si_3–MoB–$MoSi_2$	Mo_5Si_3 + Mo_5SiB_2 + MoB + $MoSi_2$
33	28.2	13.3	+ Mo_5Si_3–MoB + little Mo_5Si_3–MoB–$MoSi_2$	Mo_5Si_3 + Mo_5SiB_2 + MoB + $MoSi_2$
34	7.4	23.8	+ Mo_2B + Mo_{SS}–Mo_5SiB_2 + little Mo_{SS}–Mo_5SiB_2–Mo_3Si	Mo_{SS} + Mo_3Si + Mo_5SiB_2 + Mo_2B
35	8.1	22.6	+ Mo_{SS}–Mo_5SiB_2 + Mo_{SS}–Mo_5SiB_2–Mo_3Si	Mo_{SS} + Mo_3Si + Mo_5SiB_2
36	9.3	21.7	+ Mo_{SS}–Mo_5SiB_2 + little Mo_{SS}–Mo_5SiB_2–Mo_3Si	Mo_{SS} + Mo_3Si + Mo_5SiB_2

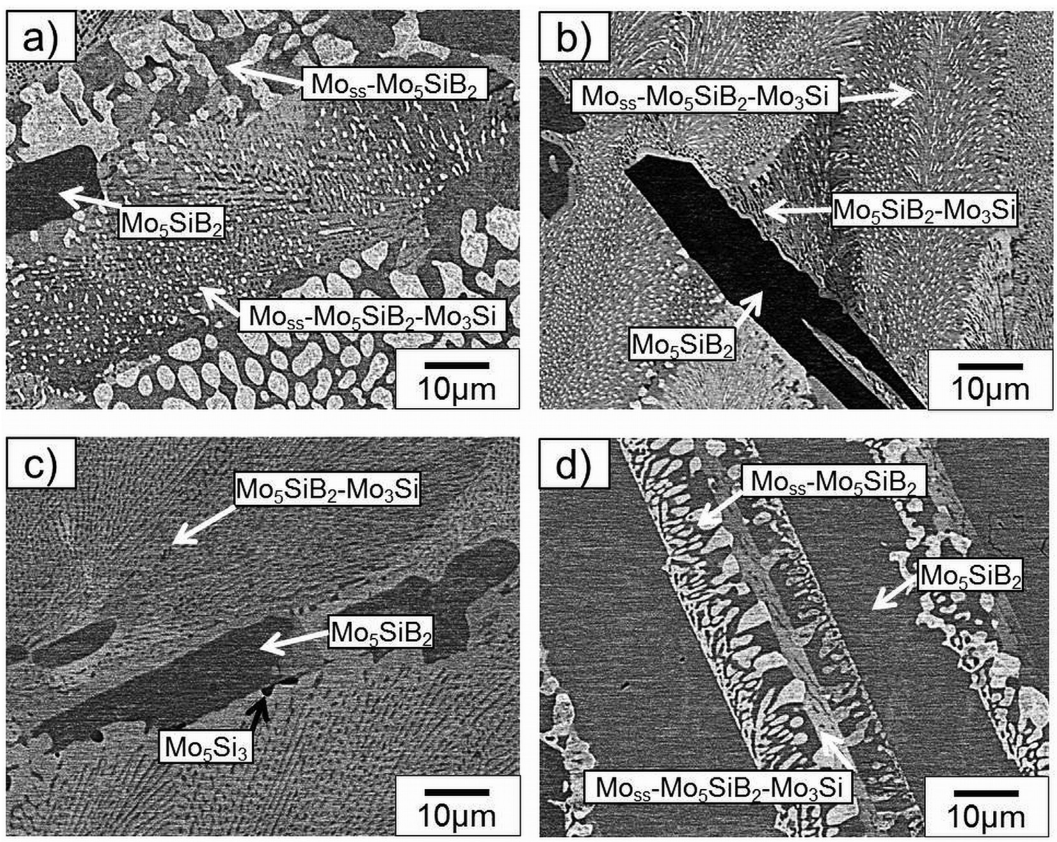

Fig. 5. SEM-BSE images of a) Mo–15Si–10B (#21), b) Mo–16.9Si–7.4B (#26), c) Mo–21Si–7.2B (#28) and d) Mo–9.3Si–21.7B (#36).

Table 4
Arc-melted alloys solidifying with the Mo_5Si_3 primary phase.

Alloy #	at.% Si	at.% B	Primary Mo_5Si_3 + further solidifying phases	Phases by XRD
37	21.8	6.2	+ Mo_5SiB_2–Mo_3Si	Mo_3Si + Mo_5Si_3 + Mo_5SiB_2
38	22.4	6.2	+ Mo_5SiB_2–Mo_3Si	Mo_3Si + Mo_5Si_3 + Mo_5SiB_2
39	22.8	6.0	+ Mo_5SiB_2–Mo_3Si	Mo_3Si + Mo_5Si_3 + Mo_5SiB_2
40	24.0	5.0	+ Mo_5SiB_2–Mo_3Si	Mo_3Si + Mo_5Si_3 + Mo_5SiB_2
41	25.0	5.0	+ Mo_5SiB_2–Mo_3Si	Mo_3Si + Mo_5Si_3 + Mo_5SiB_2
42	23.8	4.6	+ Mo_3Si + Mo_5SiB_2–Mo_3Si	Mo_3Si + Mo_5Si_3 + Mo_5SiB_2
43	21.9	7.3	+ Mo_5Si_3–Mo_5SiB_2 + Mo_5SiB_2–Mo_3Si	Mo_3Si + Mo_5Si_3 + Mo_5SiB_2
44	28.2	11.5	+ Mo_5Si_3–MoB + Mo_5Si_3–Mo_5SiB_2 + Mo_5Si_3–MoB–$MoSi_2$	Mo_5Si_3 + Mo_5SiB_2 + MoB + $MoSi_2$
45	29.1	11.4	+ Mo_5Si_3–MoB + Mo_5Si_3–Mo_5SiB_2 + little Mo_5Si_3–MoB–$MoSi_2$	Mo_5Si_3 + MoB + $MoSi_2$
46	28.8	12.4	+ Mo_5Si_3–MoB + Mo_5Si_3–MoB–$MoSi_2$	Mo_5Si_3 + MoB + $MoSi_2$
47	29.0	12.9	+ Mo_5Si_3–MoB + Mo_5Si_3–MoB–$MoSi_2$	Mo_5Si_3 + Mo_5SiB_2 + MoB + $MoSi_2$

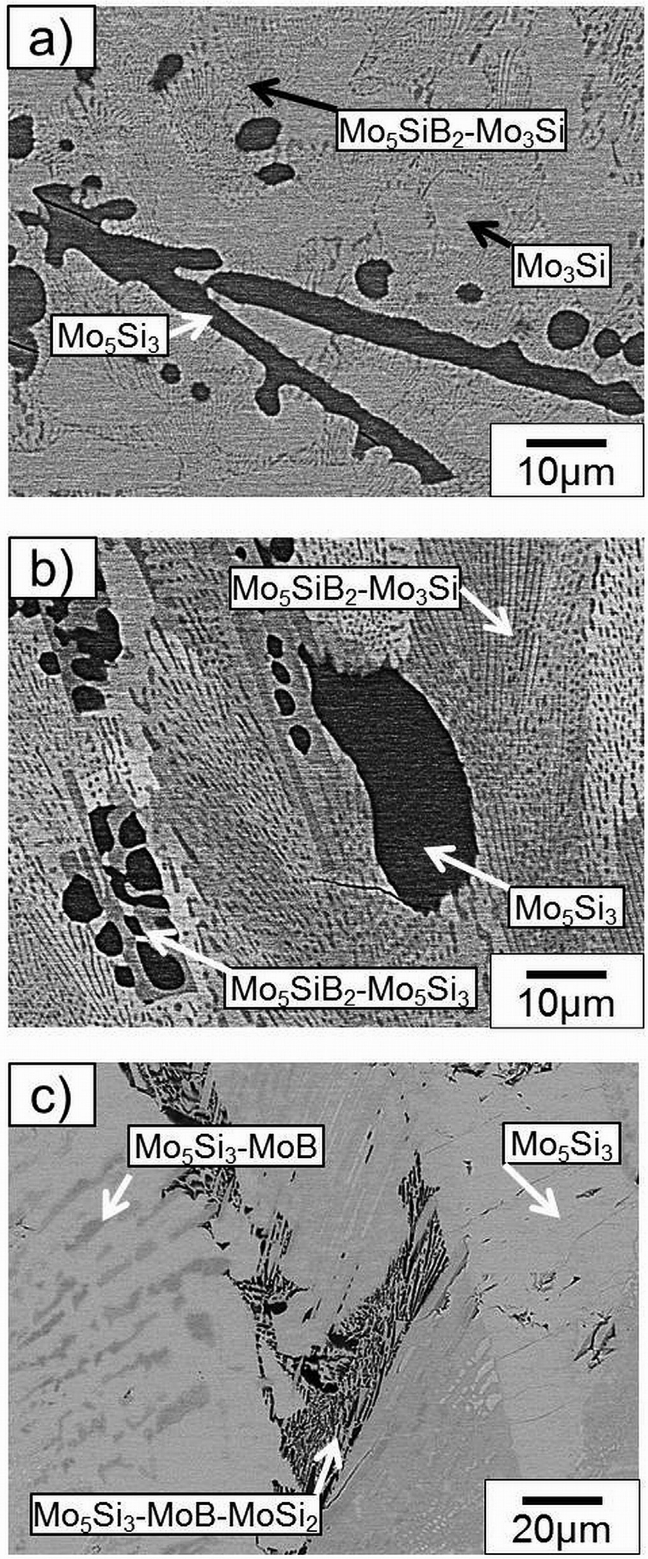

Fig. 6. SEM-BSE images of a) Mo−23.8Si−4.6B (#42), b) Mo−21.9Si−7.3B (#43) and c) Mo−28.8Si−12.4B (#46).

listed in Table 4. The primary Mo_5Si_3 solidification field covers a broad compositional field which reaches from the Mo_3Si to the $MoSi_2$ compositions on the binary Mo−Si side and expends into the ternary field up to its maximum B concentration at the U_3 four-phase reaction. For the present investigation only the Mo-rich part will be investigated and discussed.

The representative microstructures are shown in Fig. 6. The alloy Mo−23.8Si−4.6B (#42) is shown in Fig. 6a in which the black primary Mo_5Si_3 dendrites are clearly visible. The microstructure possesses secondary Mo_3Si crystals which might be results of undercooling effects during arc-melting and thus, a two-phase Mo_5SiB_2−Mo_3Si eutectic can be observed.

The solidification path of alloy Mo−21.9Si−7.3B (#43), Fig. 6b also ends along the two-phase Mo_5SiB_2−Mo_3Si valley. However, the reaction is preceded by the Mo_5SiB_2−Mo_5Si_3 mono-variant eutectic line until the reaction U_4 is reached.

Close to the U_4 reaction, the alloy composition of Mo−28.8Si−12.4B (#46), Fig. 6c, follows the binary line of Mo_5Si_3−MoB before the solidification ends in a very fine three-phase microstructure consisting of Mo_5Si_3, MoB and $MoSi_2$. According to Nunes et al. [15], Katrych et al. [16] and Yang and Chang [18] these three phases form a second ternary eutectic which is, however, not shown in Fig. 1 anymore.

4.5. Alloys with Mo2B primary phase

The alloys of investigation that solidify with a primary Mo_2B phase are listed in Table 5. On the Mo−B binary side this solidification area is confined by the binary eutectic reaction of Mo_{SS}−Mo_2B at 23 at.% B and is in equilibrium with the liquid phase up to 30 at.% B [5]. The class II reactions U_1 and U_2 define this solidification region regarding the ternary compositions when Si is added. Exemplarily, microstructures of alloys solidifying within the Mo_2B region are presented in Fig. 7.

The solidification of alloy Mo−1.3Si−21B (#48) in Fig. 7a) proceeds along the binary eutectic valley of Mo_{SS}−Mo_2B. After undergoing the reaction $L + Mo_2B \leftrightarrow Mo_{SS} + Mo_5SiB_2$ (U_2) with a weak peritectic character the solidification ends along the two-eutectic of Mo_{SS} and Mo_5SiB_2.

The two alloys Mo−5.1Si−20.1B (#49) and Mo−8.7Si−15.7B (#50), which are shown in Fig. 7b and c, solidify via a similar solidification path as compared to alloy #48 described before. However, the remaining melt reaches the ternary eutectic point and thus, ternary eutectic grains of Mo_{SS}−Mo_5SiB_2−Mo_3Si are observed in these two alloys, respectively.

Due to the secondary crystallization of the Mo_5SiB_2 phase in alloys Mo−7.4Si−21.9B (#51), their solidification path avoid the Mo_2B−Mo_5SiB_2 line and solidifies manly along the two-phase eutectic Mo_{SS}−Mo_5SiB_2 and minor formation of the ternary eutectic instead.

4.6. Alloys with MoB primary phase

Alloys taken from the primary MoB solidification area are listed in Table 6 and were chosen with special attention to the class II reaction U_3, respectively. MoB solidifies congruently at its stoichiometric composition and is bound by the two peritectic reactions $L + MoB \leftrightarrow Mo_2B$ at 30 at.% B and $L + MoB \leftrightarrow MoB_2$ at 70 at.% B on the binary Mo−B side [5]. Unlike the primary solidification field discussed so far, the MoB region extends deeply into the ternary Mo−Si−B system. Since a local maximum (saddle point) was identified along the two-phase eutectic valley of Mo_5SiB_2 and MoB, the solidification area of primary MoB crystallization can be subdivided in a Mo−B-rich portion including the U_1-type reaction and a Mo−Si-rich section which includes the U_3 reaction [15] which results in a ternary eutectic reaction of Mo_5Si_3−MoB−$MoSi_2$, if the Si concentration is further increased. Finally, the U-type reaction $L + MoB \leftrightarrow MoB_2 + MoSi_2$ borders this primary area at intermediate B and Si concentrations and is not in focus of the present investigations.

The alloy Mo−28.3Si−14B (#56), Fig. 8a, is an example which is

Table 5
Arc-melted alloys solidifying with the Mo_2B primary phase.

Alloy #	at.% Si	at.% B	Primary Mo_2B + further solidifying phases	Phases by XRD
48	1.3	21.0	+ Mo_{SS}–Mo_2B + Mo_{SS}–Mo_5SiB_2	Mo_{SS} + Mo_5SiB_2 + Mo_2B
49	5.1	20.1	+ Mo_{SS}–Mo_2B + Mo_{SS}–Mo_5SiB_2 + little Mo_{SS}–Mo_5SiB_2–Mo_3Si	Mo_{SS} + Mo_3Si + Mo_5SiB_2 + Mo_2B
50	8.7	15.7	+ Mo_{SS}–Mo_2B + Mo_{SS}–Mo_5SiB_2 + little Mo_{SS}–Mo_5SiB_2–Mo_3Si	Mo_{SS} + Mo_3Si + Mo_5SiB_2 + Mo_2B
51	7.4	21.9	+ Mo_{SS}–Mo_2B + Mo_{SS}–Mo_5SiB_2 + little Mo_{SS}–Mo_5SiB_2–Mo_3Si	Mo_{SS} + Mo_3Si + Mo_5SiB_2 + Mo_2B

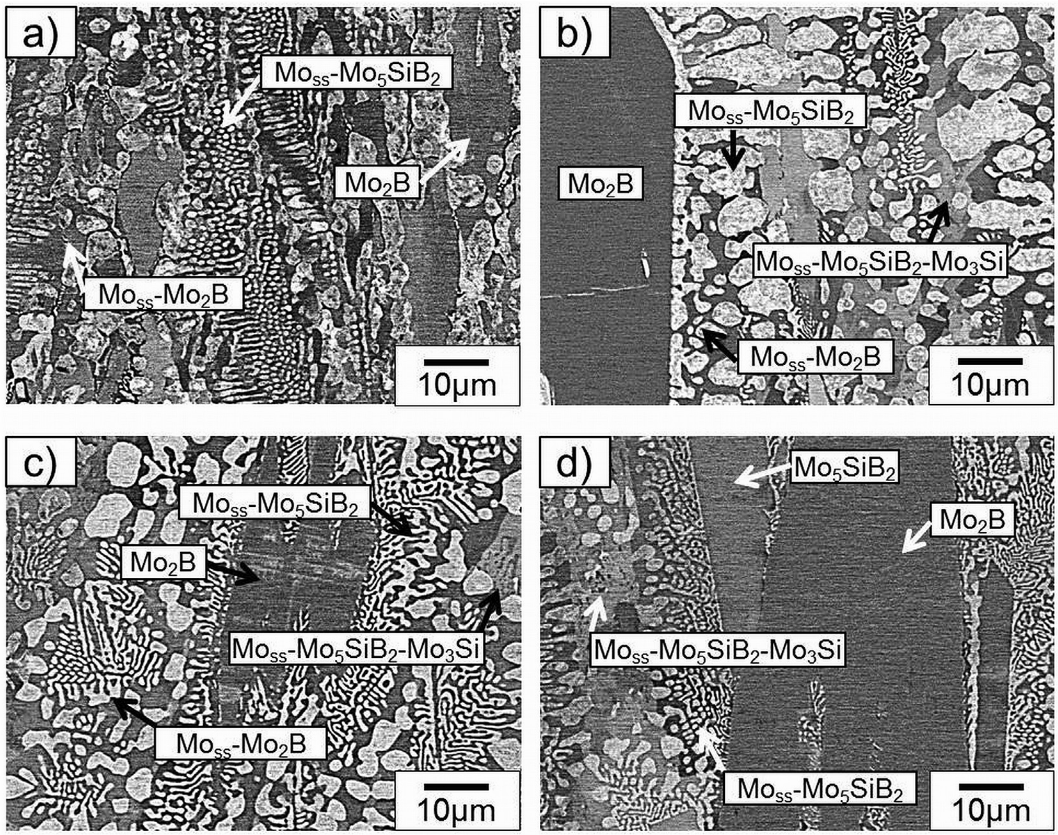

Fig. 7. SEM-BSE images of a) Mo–1.3Si–21B (#48), b) Mo–5.1Si–20.1B (#49), c) Mo–8.7Si–15.7B (#50) and d) Mo–7.4Si–21.9B (#51).

close to the U_3 reaction in which the primary MoB dendrites decompose in a halo of Mo_5Si_3 leading to the two-phase Mo_5Si_3–MoB eutectic and some grains of a ternary Mo_5Si_3–MoB–$MoSi_2$ eutectic. The Mo_5Si_3–MoB valley seems to be preferred since no evidence for the two-phase Mo_5SiB_2–MoB or Mo_5SiB_2 decomposition were observed in the alloy and the MoB liquidus surface is rather steep towards the reaction point of U_3, oppressing the mono-variant line of Mo_5SiB_2–MoB.

Alloy Mo–7.6Si–26.6B (#59) is shown in Fig. 8b. The primary formation of the MoB phase in this alloy is followed by a secondary formation of relatively large Mo_5SiB_2 crystals. Due to the relatively shallow Mo_5SiB_2 liquidus surface the alloy seems to suppress the class II reaction of L + Mo_2B ↔ Mo_{SS} + Mo_5SiB_2 and thus, the solidification path id not following the Mo_2B–Mo_5SiB_2 eutectic valley. Consequently, the solidification path proceeds similar as Mo_5SiB_2 primary solidifying alloys, i.e. like alloy Mo–9.3Si–21.7B (#36), showing the two-phase eutectic of Mo_{SS}–Mo_5SiB_2 and small regions of the ternary eutectic.

5. Discussion

The present investigations on the microstructure evolution of

Table 6
Arc-melted alloys solidifying with the MoB primary phase.

Alloy #	at.% Si	at.% B	Primary MoB + further solidifying phases	Phases by XRD
52	26.3	15.1	+ Mo_5SiB_2 + Mo_5Si_3–MoB + Mo_5Si_3–MoB–$MoSi_2$	Mo_5Si_3 + Mo_5SiB_2 + MoB + $MoSi_2$
53	26.0	16.8	+ Mo_5Si_3–MoB + Mo_5Si_3–MoB–$MoSi_2$	Mo_5Si_3 + MoB + $MoSi_2$
54	27.3	15.5	+ Mo_5Si_3–MoB + Mo_5Si_3–MoB–$MoSi_2$	Mo_5Si_3 + MoB + $MoSi_2$
55	27.9	15.4	+ Mo_5Si_3–MoB + Mo_5Si_3–MoB–$MoSi_2$	Mo_5Si_3 + MoB + $MoSi_2$
56	28.3	14.0	+ Mo_5Si_3–MoB + Mo_5Si_3–MoB–$MoSi_2$	Mo_5Si_3 + MoB + $MoSi_2$
57	29.1	13.7	+ Mo_5Si_3–MoB + Mo_5Si_3–MoB–$MoSi_2$	Mo_5Si_3 + MoB + $MoSi_2$
58	9.3	24.3	+ Mo_{SS}–Mo_5SiB_2 + Mo_{SS}–Mo_5SiB_2–Mo_3Si	Mo_{SS} + Mo_3Si + Mo_5SiB_2 + MoB
59	7.6	26.6	+ Mo_5SiB_2 + Mo_{SS}–Mo_5SiB_2 + Mo_{SS}–Mo_5SiB_2–Mo_3Si	Mo_{SS} + Mo_3Si + Mo_5SiB_2 + MoB

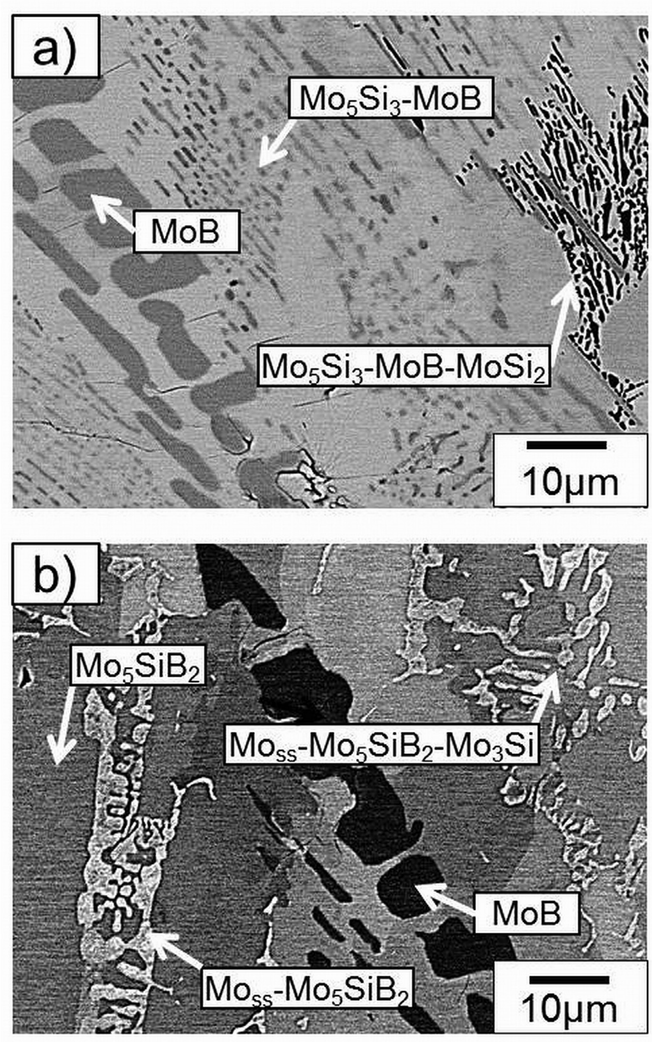

Fig. 8. SEM-BSE images of a) Mo–28.3Si–14B (#56) and b) Mo–7.6Si–26.6B (#59).

Mo-rich Mo–Si–B alloys are in good agreement with previous experimental results on the solidification behavior and liquidus projections published in the literature [10,11,15,16,18,19]. In general, the obtained results confirm the six primary solidification regions and the four-phase class II and class I reactions reported by Nunes et al. [15] and Yang and Chang [18,19]. Despite the fact of a general agreement on the liquidus surface there still seem to exist different interpretations regarding the size and extension of the primary Mo_3Si field. The present experimental study revealed a much larger Mo_3Si primary solidification field as reported before [15,16,18,19] which is the biggest and apparent difference to the previous reported liquidus projections. In principle, its extension follows the Yang and Chang [18,19] calculation being relatively rich in its B concentration (about 7 at.%). On the other hand it broadens into the ternary diagram as proposed by Nunes et al. [15] and seems to open and expends clearly along the Si axis having it's maximum expansion along the binary Mo_5SiB_2–Mo_3Si eutectic valley. Thus, the present solution is a combination of earlier findings which draws a much clearer picture of the Mo_5SiB_2–Mo_3Si eutectic valley. The length and position of this eutectic line can now be redetermined considering the new findings. While its presence was almost not visible in the Yang and Chang [18,19] thermodynamic prediction, it tended to decrease in its B concentration with increasing Si according to Nunes et al. [15] and Katrych et al. [16]. The present experimental results show, however, no clear dependence on the B concentration and imply that the Mo_5SiB_2–Mo_3Si eutectic line is almost parallel to the binary Mo–Si system.

As first results one can state from the experimental investigations summarized in Fig. 9: (i) a much larger Mo_3Si primary solidification area than reported in previous studies on the liquidus projection of the Mo-rich Mo–Si–B system [15,16,18,19] and thus, (ii) the Mo_5SiB_2–Mo_3Si eutectic line connecting the ternary eutectic point E_t and the mono-variant class II reaction U_4 is found to be much longer than in those investigations before. One has to note here that the position of the U_4 reaction is a result of the interpolation of the primary crystal solidifications in the alloys investigated and cannot be measured directly. The present findings of a much broader Mo_3Si primary solidification field were possible, since the ternary eutectic point could be clearly identified to contain 17 ± 1 at.% silicon and 7.5 ± 0.5 at.% boron.

These new findings also have an influence on the ternary eutectic reaction, which is located in the so-called Berczik triangle [29] and consists of the Mo_{SS} and the intermetallic phases Mo_5SiB_2 and Mo_3Si. There is a common consent in the scientific Mo–Si–B community which clearly pointed out the importance of alloys taken from this part of the phase diagram, due to their unique and adjustable properties [30]. Thus, the lowest melting point and a deeper understanding of the solidification behavior of near-eutectic alloys in such an important phase field will offer new applications for Mo–Si–B alloys beyond the processing route of casting and powder metallurgy, i.e., for additive manufacturing processes [31].

According to the present experimental setup a few near-ternary eutectic alloys which are located either in the Mo_{SS} primary field (alloys #6, #7 and #8), the Mo_3Si field (alloy #18) or the Mo_5SiB_2 primary field (alloys #22 and #26) can be identified. All alloys feature a relatively small volume fraction of their individual primary phases and consist mainly of ternary eutectic grains and are therefore treated as near-eutectic alloys. The obtained results are in good correlation with previous literature findings. Microstructure analysis by Ha et al. [10], for example, measured the concentration of the ternary eutectic grains and mentioned a noticeable experimental scatter which had been attributed to undercooling effect mainly caused by the steep Mo_{SS} primary liquidus surface and the relatively flat and shallow liquidus surface of the intermetallic phases Mo_5SiB_2 and Mo_3Si. The near-eutectic alloys identified in the present study represent the ternary eutectic concentrations measured via EPMA by Ha et al. [10]. In combination with the present results, the ternary eutectic point can be determined to be located between 17 ± 1 at.% Si and 7.5 ± 0.5 at.% B which is also resembled by the present experimental results. Compared to Yang and Chang's thermodynamic calculations [18,19] the experimental results on the ternary eutectic point have almost the same B concentration but differ in the Si concentration, which is slightly Si-lean as the calculation is predicting. This explains the extended Mo_3Si primary solidification field reported in the present work.

Since the liquidus surfaces of the primary solidification areas of Mo_{SS}, Mo_3Si, Mo_5SiB_2 and Mo_5Si_3 have different slopes, undercooling strongly affects the solidification path. If we assume a ternary eutectic reaction within the Berczik triangle [29], different slopes of the liquidus surfaces will have an influence on the coupled growth of eutectic phases. To describe these possible influences a binary eutectic system should serve as an example.

At first we will assume a simple binary eutectic which is symmetric over its eutectic reaction, meaning both phases are equally distributed within the eutectic microstructure. The coupled zone is described by the temperature-concentration zone in which the combined eutectic growth of both phases proceeds faster than the growth of the individual primary phases. Hence, the eutectic growth rate in systems with components that have nearly equal values for their entropy of fusion, ΔS, is higher than the growth of

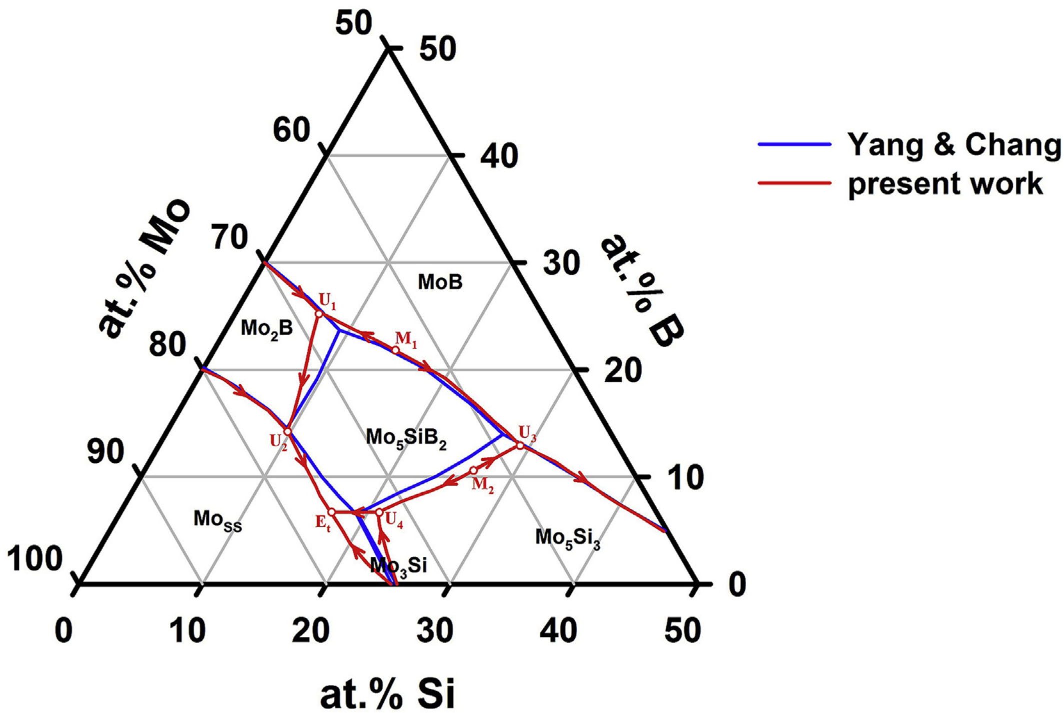

Fig. 9. Comparison of the Mo—Si—B liquidus projection by Yang and Chang [18,19] with the experimental results obtained in the present study.

the primary phases and thus preferred. This is, indeed, the case for normal (symmetric) eutectic systems.

If, however, the components strongly differ in their entropy of fusion (i.e., $\Delta S_\alpha < \Delta S_\beta$, while considering α and β schematically as solid phases), the component with the smaller entropy of fusion tends to grow faster than the eutectic reaction. This describes an asymmetric ternary system in which the volume fraction of e.g. the β-phase is higher than the α-phase. In this case, the eutectic composition must be shifted towards the component having the higher entropy of fusion to get a nearly equal growth rate of both phases and thus reaching a zone of coupled growth. Hence, if eutectic systems including one phase of a high ΔS value (in the present example the β-phase) solidify with a sufficiently high solidification rate, a hypereutectic composition can be attained resulting in a much higher volume fraction of this phase than the eutectic equilibrium would suggest. The formation of secondary α-phase is also possible in this case. According to Kurz and Sahm [28] an asymmetric coupled zone of a hypereutectic alloy can result in a preferential primary growth of the β-phase at low solidification rates and thus, at small ΔT values. By increasing the undercooling temperature ΔT a coupled eutectic growth regime can be reached at high solidification rate (that refers to a strong undercooling) even the α-phase could be promoted. Consequently, the growth kinetics strongly affects the stability of the coupled eutectic growth [28].

If one now transfers these considerations on simple binary systems to ternary systems the situation can get even more complicated. The Mo—Si—B system is asymmetric over its ternary eutectic point, only the Mo_{SS} primary solidification surface has a steep slope while the primary solidification surfaces of Mo_3Si and Mo_5SiB_2 (Mo_5Si_3, too) are relatively shallow and flat. Kurz and Sahm [28] might help to explain why the ternary eutectic compositions measured by Ha et al. [10] scatter around the expected (real) ternary eutectic composition. Due to the asymmetric character of the Mo_{SS}—Mo_5SiB_2—Mo_3Si eutectic reaction and the strong undercooling caused by the arc-melting process (with high undercooling ΔT) the eutectic reaction is overshot in each of the alloys investigated. The scatter can then be explained by the formation of many eutectic cells resulting from slightly different cooling paths. As a direct result of this effect, these eutectic cells differ in their individual eutectic compositions due to very local changes in the liquid concentration - the real eutectic composition could therefore not be determined precisely.

Taking all these considerations and new findings into account, they allow to draw a new, revised and slightly different version of the Mo—Si—B liquidus surface as compared to the present literature, which is shown in Fig. 9.

The mono-variant reaction U_2 is relatively well-known due to investigations on the Mo_{SS}—Mo_5SiB_2 pseudo-binary phase diagram [6—9]. Hence, its position or concentration in the present study was adopted from the latest experimental results presented by Ha et al. [10]. The mono-variant reactions U_1 and U_3 were determined by the identification of the primary crystallization areas of the present alloys and deduced by an interpolation of the obtained results.

A more detailed analysis of the present liquidus surface and the solidification paths of the alloys investigated can be obtained by employing the Alkemade theorem. A first local maximum (M_1) in the Mo-rich part of the Mo—Si—B liquidus surface should exist along the eutectic-type mono-variant line which separates the two primary solidification areas of the MoB phase and the Mo_5SiB_2 phase. According to the theorem a second maximum (M_2) should thus exist along the Mo_5SiB_2—Mo_5Si_3 eutectic valley. Both local maxima were also reported in the literature [10,15,16,18,19]. According to the liquidus projections proposed by Nunes et al. [15] and Katrych et al. [16] a third maximum (their m_2 or max_2, respectively) should exist along the mono-variant line between MoB and Mo_5Si_3, which however, was not corroborated by Yang and Chang [18,19] or Ha et al. [10]. Thus, the present work reveals a U_3 reaction of L + Mo_5SiB_2 ↔ MoB + Mo_5Si_3 (contrary to Nunes et al. [15] and L + β-MoB ↔ Mo_5Si_3 + Mo_5SiB_2. Since MoB, Mo_5SiB_2 and Mo_5Si_3 exist in a quite extended homogeneity range, however, the precise position of the maxima cannot be directly predicted by the theorem (as mentioned earlier), which has direct influence on the U_3 four-phase reaction.

If one draws the Alkemade line between the stoichiometric

Mo_5SiB_2 and Mo_3Si phases as previously shown above in Fig. 2 it leads to a similar situation like for Yang and Chang's thermodynamic calculation. Again, the Alkemade line does not intersect with the corresponding Mo_5SiB_2—Mo_3Si eutectic line. However, the Alkemade theorem states that, if a boundary curve (here the Mo_5SiB_2—Mo_3Si eutectic line) does not intersect with the Alkemade line an extension to the pertinent Alkemade line can be made [20,25]. Hence, this is the case in the present situation and it becomes obvious that both reactions U_4 and E_t are located left of the Alkemade line. It turns out that the solidification sequence can now be interpreted using the same solidification sequence as for Yang and Chang's approach which had been confirmed experimentally by Ha et al. [10]: the mono-variant reaction L + Mo_5Si_3 ↔ Mo_3Si + Mo_5SiB_2 precedes the ternary eutectic reaction L ↔ Mo_{SS} + Mo_3Si + Mo_5SiB_2.

6. Summary and conclusions

In the present study the microstructure evolution during solidification in a wide concentration range of the ternary Mo—Si—B system was investigated. The obtained results can be summarized with the following bullet points.

1. The liquidus projection of the Mo-rich portion of the Mo—Si—B system has critically reinvestigated. The Alkemade theorem was used to take a closer look into published liquidus projections, solidification paths and thus the solidification sequence. The Alkemade line between the two intermetallic phases Mo_5SiB_2 and Mo_3Si is of special importance for the four-phase reactions named as U_4 and the ternary eutectic reaction E_t. The present work agrees with the solidification sequence provided by Nunes et al. [15] and Yang and Chang [18,19] while discussing the discrepancies with Katrych et al.'s [16] reaction sequence very critically. The analysis using the Alkemade theorem is also in agreement with the experimental results presented in this work.
2. In general, the present experiments on the Mo—Si—B liquidus projection are in good agreement with the literature investigations [10,15,16,18,19]. However, a much larger primary solidification area of the Mo_3Si phase was determined as mentioned in the earlier studies which has a significant impact on the microstructure evolution of alloys in this compositional range.
3. Special attention was paid on the identification of the ternary eutectic point in the liquidus projection which differs considerably from previous reported studies [15,16,18,19]. The Mo_{SS}—Mo_5SiB_2—Mo_3Si eutectic composition was relatively difficult to obtain due to undercooling effects during solidification using arc-melting and a water-chilled copper crucible and the topographical shape of the liquidus projection itself.
4. As a final result of the present experimental reinvestigation a revised liquidus projection is introduced based on the present experimental analyses, especially around the ternary eutectic reaction.

Data availability

The raw/processed data required to reproduce these findings cannot be shared at this time as the data also forms part of an ongoing study.

CRediT authorship contribution statement

G. Hasemann: Writing - original draft, Writing - review & editing. **S. Ida:** Writing - original draft. **L. Zhu:** Writing - original draft. **T. Iizawa:** Investigation. **K. Yoshimi:** Supervision, Writing - review & editing. **M. Krüger:** Supervision, Writing - review & editing.

Acknowledgements

This research was partly supported by the German Federal Ministry of Education and Research (BMBF) programs "HOTWIN" (funding number 01DK13030), "FlexiDS" (funding number 05K16NMA), the Advanced Low Carbon Technology Research and Development Program (ALCA) of the Japan Science and Technology (JST) (funding number JPMJAL1303) and International Joint Graduate Program in Materials Science (GP-MS) of Tohoku University. Financial support of the Methodisch-Diagnostisches Zentrum Werkstoffprüfung (MDZWP) e.V., Magdeburg, Germany is greatly acknowledged. LZ also appreciates a financial support provided by the China Scholarship Council (CSC).

References

[1] P. Jéhanno, M. Heilmaier, H. Saage, M. Böning, H. Kestler, J. Freudenberger, S. Drawin, Assessment of the high temperature deformation behavior of molybdenum silicide alloys, Mater. Sci. Eng. A 463 (2007) 216—223, https://doi.org/10.1016/j.msea.2006.08.125.
[2] T.A. Parthasarathy, M.G. Mendiratta, D.M. Dimiduk, Oxidation mechanisms in Mo-reinforced Mo5SiB2 (T2)—Mo3Si alloys, Acta Mater. 50 (2002) 1857—1868.
[3] M.G. Mendiratta, T.A. Parthasarathy, D.M. Dimiduk, Oxidation behavior of aMo—Mo3Si—Mo5SiB2 (T2) three phase system, Intermetallics 10 (2002) 225—232.
[4] D. Shifler, O.M. Strbik, N13A-T012: mechanical property characterization and modeling for structural Mo-Si-B alloys for high temperature applications, Dep. Navy SBIR/STTR Transit. Program, ONR Approv. (2017) 3474. # 43-2203-16.
[5] K.E. Spear, P.K. Liao, The B-Mo (boron-molybdenum) system, Bull. Alloy Phase Diagrams 9 (1988) 457—466.
[6] R. Sakidja, H. Sieber, J.H. Perepezko, The formation of Mo precipitates in a supersaturated Mo5SiB2 intermetallic phase, Philos. Mag. Lett. 79 (1999) 351—357.
[7] R. Sakidja, J. Myers, S. Kim, J.H. Perepezko, The effect of refractory metal substitution on the stability of Mo(ss) + T2 two-phase field in the Mo-Si-B system, Int. J. Refract. Metals Hard Mater. 18 (2000) 193—204.
[8] S.H. Ha, K. Yoshimi, K. Maruyama, R. Tu, T. Goto, Phase formation and solidification routes near Mo-Mo5SiB2 eutectic point in Mo-Si-B system, Mater. Trans. 51 (2010) 1699—1704, https://doi.org/10.2320/matertrans.M2010153.
[9] K. Yoshimi, S.H. Ha, K. Maruyama, R. Tu, T. Goto, Microstructural evolution of Mo-Si-B ternary alloys through heat treatment at 1800°C, Adv. Mater. Res. 278 (2011) 527—532, https://doi.org/10.4028/www.scientific.net/AMR.278.527.
[10] S.H. Ha, K. Yoshimi, J. Nakamura, T. Kaneko, K. Maruyama, R. Tu, T. Goto, Experimental study of Moss—T2, Moss—Mo3Si—T2, and Mo3Si—T2 eutectic reactions in Mo-rich Mo—Si—B alloys, J. Alloy. Comp. 594 (2014) 52—59, https://doi.org/10.1016/j.jallcom.2014.01.089.
[11] G. Hasemann, D. Kaplunenko, I. Bogomol, M. Krüger, Near-eutectic ternary Mo-Si-B alloys: microstructures and creep properties, J. Miner. Met. Mater. Soc. 68 (2016) 2847—2853, https://doi.org/10.1007/s11837-016-2073-0.
[12] G. Hasemann, I. Bogomol, D. Schliephake, P.I. Loboda, M. Krüger, Microstructure and creep properties of a near-eutectic directionally solidified multiphase Mo—Si—B alloy, Intermetallics 48 (2014) 28—33, https://doi.org/10.1016/j.intermet.2013.11.022.
[13] H. Nowotny, E. Dimakopoulou, H. Kudielka, Untersuchungen in den Dreistoffsystemen: Molybdän-Silizium-Bor , Wolfram-Silizium-Bor und in dem System: VSi2-TaSi2, Mh, Chem 88 (1957) 180—192.
[14] S.H. Ha, K. Yoshimi, K. Maruyama, R. Tu, T. Goto, Compositional regions of single phases at 1800°C in Mo-rich Mo-Si-B ternary system, Mater. Sci. Eng. A 552 (2012) 179—188, https://doi.org/10.1016/j.msea.2012.05.028.
[15] C.A. Nunes, R. Sakidja, Z. Dong, J.H. Perepezko, Liquidus projection for the Mo-rich portion of the Mo-Si-B ternary system, Intermetallics 8 (2000) 327—337.
[16] S. Katrych, A. Grytsiv, A. Bondar, P. Rogl, T. Velikanova, M. Bohn, Structural materials: metal-silicon-boron: on the melting behavior of Mo-Si-B alloys, J. Alloy. Comp. 347 (2002) 94—100, https://doi.org/10.1016/S0925-8388(02)00676-X.
[17] M. Pirani, H. Alterthum, Über eine Methode zur Schmelzpunktbestimmung an hochschmelzenden Metallen, Z. Elektrochem. Angew. Phys. Chem. 29 (1923) 5—8.
[18] Y. Yang, Y.A. Chang, Thermodynamic modeling of the Mo—Si—B system, Intermetallics 13 (2005) 121—128, https://doi.org/10.1016/j.intermet.2004.06.007.
[19] Y. Yang, Thermodynamic Modeling and Experimental Investigation of the Mo-Si-B-Ti Quaternary System, PhD Thesis, University of Wisconsin - Madison, 2004, https://doi.org/10.1016/j.jallcom.2014.01.062.
[20] A.C. van Rijn van Alkemade, Graphical treatment of some thermodynamic

problems with equilibrium states of salt solutions with solid phases, Z. Phys. Chem. 11 (1893) 289–327.
[21] J.H. Perepezko, R. Sakidja, S. Kim, Phase stability in processing and microstructure control in high temperature Mo-Si-B alloys, Mater. Res. Soc. Symp. Proc. 646 (2001) N4.5.1–N4.5.12, https://doi.org/10.1557/PROC-646-N4.5.1.
[22] R. Sakidja, J.H. Perepezko, S. Kim, N. Sekido, Phase stability and structural defects in high-temperature Mo–Si–B alloys, Acta Mater. 56 (2008) 5223–5244, https://doi.org/10.1016/j.actamat.2008.07.015.
[23] A.B. Gokhale, G.J. Abbaschian, The Mo-Si (Molybdenum-Silicon) system, J. Phase Equilibria 12 (1991) 493–498, https://doi.org/10.1007/BF02645979.
[24] H. Choe, D. Chen, J.H. Schneibel, R.O. Ritchie, Ambient to high temperature fracture toughness and fatigue-crack propagation behavior in a Mo-12Si-8.5B (at.%) intermetallic, Intermetallics. http://www.sciencedirect.com/science/article/pii/S0966979501000085, 2001 (accessed October 25, 2013)319-329.
[25] D.R.F. West, Ternary Equilibrium Diagrams, 2. Edition, Springer, Netherlands, Dordrecht, 1982, https://doi.org/10.1007/978-94-009-5910-1.
[26] F.E.E. Lamplough, J.T. Scott, The growth of metallic eutectics, Proc. R. Soc. Lond. - Ser. A Contain. Pap. a Math. Phys. Character 90 (1914) 600–604, https://doi.org/10.1098/rspa.1914.0092.
[27] F. Stein, C. He, O. Prymak, S. Voß, I. Wossack, Phase equilibria in the Fe-Al-Nb system: solidification behaviour, liquidus surface and isothermal sections, Intermetallics 59 (2015) 43–58, https://doi.org/10.1016/j.intermet.2014.12.008.
[28] W. Kurz, P.R. Sahm, Kopplungsgrad des eutektischen Wachstums, in: Gerichtete Erstarrung Eutektischer Werkstoffe, Springer-Verlag, Berlin, Heidelberg, New York, 1975, pp. 106–116.
[29] D.M. Berczik, US Patent 5,595,616 and 5,693,156, US Pat. 5,595,616; 5,693,156, East Hartfort, United Technol. Corp. (1997).
[30] J.H. Schneibel, Mo-Si-B Alloy Development, in: Proc. 17th Annu. Conf. Foss. Energy Mater., 2003, pp. 3–9 [Baltimore, Maryland]. (2003).
[31] J. Schmelzer, S.-K. Rittinghaus, A. Weisheit, M. Stobik, J. Paulus, K. Gruber, E. Wessel, C. Heinze, M. Krüger, Printability of gas atomized Mo-Si-B powders by laser metal deposition, Int. J. Refract. Metals Hard Mater. 78 (2019) 123–126, https://doi.org/10.1016/j.ijrmhm.2018.08.016.